Bol. Soc. Paran. Mat.
©SPM – E-ISSN-2175-1188
SPM: www.spm.uem.br/bspm

(3s.) **v. 2026 (44) 4** : 1–27.
ISSN-0037-8712
doi:10.5269/bspm.80150

Data-Driven Surrogate Modeling for High-Fidelity Wall Shear Stress Assessment in Idealized Cerebral Aneurysms

Shankar Narayan S.[1]*, Modi Meet Hirenkumar[2], Nidhi S. Vaishnav[3], Saradha M.[4]

ABSTRACT: This article presents a comprehensive reduced-order modeling (ROM) framework for the rapid and accurate prediction of Wall Shear Stress (WSS) fields in idealized cerebral aneurysm geometries. Utilizing Proper Orthogonal Decomposition (POD) for efficient dimensionality reduction and a feedforward Neural Network (NN) as a surrogate model, the framework significantly reduces the computational expense of high-fidelity simulations. Key findings demonstrate that POD effectively compresses the solution space, capturing over 99% of energy with a minimal number of modes, while the NN accurately predicts POD coefficients, achieving high R-squared values. This ROM pipeline enables WSS field predictions in milliseconds, offering substantial computational efficiency without compromising accuracy. The model successfully captures the geometric sensitivity of WSS patterns, including localized peak stresses at the aneurysm dome. Clinically, this framework holds promise for accelerating rupture risk assessment, optimizing treatment planning through virtual testing, and facilitating high-throughput morphological analysis. Current limitations include simplified geometric representations, static WSS estimates, and reliance on high-fidelity training data. Future work will focus on integrating patient-specific geometries, incorporating transient hemodynamics and fluid-structure interaction, and implementing uncertainty quantification for enhanced clinical applicability.

Key Words: Cerebral aneurysms, reduced order modeling, snapshots, wall stress.

Contents

* Corresponding author.

Submitted November 11, 2025. Published February 05, 2026

1. Introduction

Natural-history studies consistently show that aneurysm rupture is linked to complex interactions among morphology, wall tissue remodeling, and local hemodynamics [1,2]. High tensile stresses accumulate where geometric irregularities concentrate blood momentum, whereas chronically low wall shear stress can trigger pro-inflammatory processes that weaken the arterial wall [3]. Traditional rupture-risk scores that rely solely on static descriptors such as diameter provide only limited guidance; this limitation has led to an increased interest in individualized biomechanical measurements, including wall stress, oscillatory shear index, and tissue strain [4]. However, calculating those metrics through full Navier-Stokes simulations remains beyond the scope of most clinical workflows [5].

The transition to biomechanics-based risk assessment relies heavily on high-fidelity computational methods, such as computational fluid dynamics (CFD) and finite element analysis (FEA), to simulate the complex interplay of blood flow and vessel wall mechanics. Full 3D simulations have matured into powerful research instruments, yet each run may demand several hours of high-performance computing time. To overcome this bottleneck, Reduced-Order Modeling (ROM) has emerged as an enabling technology [6,7]. ROMs create computationally inexpensive yet accurate representations of complex systems by drastically reducing their dimensionality.

To bypass this bottleneck, researchers have increasingly adopted reduced-order models that capture dominant flow dynamics on low-dimensional manifolds [6,7]. Parallel developments in machine learning promise to map complex input-output relationships without explicitly solving the governing equations [8,9]. Connecting these two threads–data-driven ROMs enriched by neural networks–offers a compelling path toward fast, personalized risk stratification.

Zakeri et al. indicates that the structural integrity of the aneurysm wall, quantified by metrics such as wall stress and tissue stiffness, provides a more direct and robust assessment of rupture risk than geometry alone [10]. Yadav et al. developed a computational framework demonstrating that induced stresses in the aneurysm wall increase with both diameter and blood pressure, with large, thin-walled aneurysms exhibiting the highest risk [11]. Brunel et al. provided experimental evidence showing that ruptured aneurysms are composed of biomechanically "softer" tissue compared to the stiffer tissue of unruptured aneurysms [12]. Further supporting this, Diab et al. used finite element analysis to show that wall stress distributions are highly sensitive to the wall's material properties and layered structure, reinforcing the necessity of a biomechanics-focused approach to accurately stratify risk [13].

2020 *Mathematics Subject Classification:* 92C50, 68T07, 76Z05.

Proper Orthogonal Decomposition (POD) is a powerful and widely adopted data-driven ROM technique that decomposes a high-dimensional dataset of simulation snapshots into a set of optimal, orthogonal basis functions, or "modes". These modes are ranked by their energy content, allowing the system's dominant dynamics to be captured with a very small number of basic functions [14]. Han et al. demonstrated this by developing a POD-based ROM for a patient-specific aneurysm that could rapidly evaluate hemodynamic parameters over a range of physiological conditions [14]. Critically, these POD modes are not merely mathematical abstractions; they often correspond to physically interpretable, coherent flow structures. Byrne et al. leveraged this property to classify the temporal stability of flow patterns, finding that ruptured aneurysms were associated with more unstable modes [15]. This capacity to distill complex, high-dimensional physics into a low-dimensional, physically meaningful space makes POD an ideal foundation for building computationally tractable biomechanical models. MacRaild et al. constructed a non-intrusive ROM that compresses intracranial aneurysm flow fields via POD and recovers them through neural-network interpolation, achieving accuracies approaching native simulations at a fraction of the cost [6].

In the context of aneurysm analysis, NNs have been used to predict hemodynamic parameters directly from geometric features, achieving computational speed-ups of several orders of magnitude compared to traditional CFD [16]. Li et al. developed a deep learning network that could predict the full hemodynamic field from a point cloud representation of the aneurysm geometry, drastically simplifying the analysis workflow [17]. A particularly powerful and synergistic strategy combines POD with NNs [18]. In this hybrid ROM-NN framework, POD first transforms the intractable problem of predicting a high-dimensional field into the much more manageable task of predicting a handful of POD coefficients [19]. Sarabian et al. demonstrated a sophisticated variant of this, using a physics-informed NN to fuse light clinical data with a 1-D ROM to generate high-resolution hemodynamic maps [18]. The primary challenge for all such data-driven approaches, however, remains the creation of large, diverse, and high-fidelity training datasets, an upfront computational investment that is a significant research endeavor in itself [19].

The investigation of the biomechanical environment within an aneurysm is strongly motivated by the role of Wall Shear Stress (WSS), the frictional force exerted by flowing blood on the endothelial cells lining the vessel wall [2]. Cebral et al. showed that persistently low wall shear engenders inflammatory endothelial responses, thereby accelerating aneurysm formation [20]. This theory posits that abnormally low and/or highly oscillatory WSS creates a pro-inflammatory and degenerative environment within the aneurysm sac. This leads to endothelial dysfunction, inflammatory cell infiltration, and degradation of the extracellular matrix, which collectively compromise the wall's structural integrity [21].

Despite significant advances, a critical gap remains in the clinical translation of biomechanical risk assessment. First, although wall stress serves as a more immediate indicator of mechanical failure compared to WSS, the computation of wall stress through high-fidelity finite element analysis (FEA) or fluid-structure interaction simulations is prohibitively resource-intensive for regular clinical application. Concurrently, while data-driven surrogate modelling has shown immense promise, existing efforts have predominantly focused on predicting quantities like WSS and velocity. Furthermore, the development of these powerful machine learning models has been constrained by the lack of large-scale, high-fidelity training datasets. Third, neural-network surrogates, though fast, risk violating physical constraints if not grounded in reduced-order structure. Finally, existing studies seldom deliver full-field wall stress reconstructions tailored to unseen patient anatomies in real time.

This work introduces a novel computational framework aimed at accelerating patient-specific biomechanical analysis of cerebral aneurysms. The key innovations driving this approach are:

1. **Integrated Reduced Order Modeling (ROM) and Neural Network (NN) Surrogate for Rapid Prediction:** A central innovation is the seamless integration of Proper Orthogonal Decomposition (POD) with Neural Networks to construct a highly efficient surrogate model. This ROM-NN framework enables near real-time prediction of complex wall stress distributions from geometric inputs, circumventing the need for computationally expensive full-order simulations for each new aneurysm configuration. This significantly reduces the turnaround time for obtaining crucial biomechanical insights.

2. **Systematic Data-Driven Approach for Geometric Variability:** The methodology adopts a robust data-driven paradigm by systematically generating a diverse dataset of aneurysm "snapshots." This is achieved through parametric variation of key morphological features, such as aneurysm height and width. This foundation of rich, synthetically generated data is critical for training the ROM-NN model to generalize effectively across a wide spectrum of patient-specific aneurysm shapes, addressing the challenge of limited access to extensive clinical data with corresponding high-fidelity simulations.

3. **Automated and Scalable Pipeline for Synthetic Data Generation:** An integrated MATLAB-based pipeline has been developed that links simplified, yet physics-informed, models for aneurysm geometry generation, hemodynamic parameter estimation, and subsequent wall stress calculation. This automated process efficiently produces the high-dimensional dataset required for ROM and NN training, establishing a scalable and reproducible method to build the necessary input for the machine learning component.

4. **Enhanced Efficiency for Patient-Specific Biomechanical Assessment:** By providing a rapid and robust predictive capability, this framework offers a significant advancement towards more accessible and timely patient-specific biomechanical assessment of aneurysm rupture risk. This contrasts sharply with traditional, time-consuming computational fluid dynamics (CFD) and finite element analysis (FEA) methods, thereby augmenting the practical clinical utility of such analyses in a diagnostic or pre-surgical planning context.

This paper is structured to detail the development and application of our computational framework. Section 2 elucidates the methods for aneurysm geometry generation, including 2D profile definition and 3D mesh creation via revolution. Section 3 then outlines the methodology for wall stress estimation and its role in rupture risk assessment. Following this, Section 4 elaborates on the estimation of crucial hemodynamic parameters, namely Wall Shear Stress (WSS) and Oscillatory Shear Index (OSI). The core process of generating the parametric dataset for Reduced Order Modeling is described in Section 5. Subsequently, Section 6 details the Proper Orthogonal Decomposition (POD) analysis for dimensionality reduction and mode interpretation. Section 7 presents the architecture, training, and evaluation of the Neural Network surrogate model. Finally, Section 8 provides results and discussions, Section 9 validates the surrogate model's performance, and Section 10 concludes the paper with key findings, clinical implications, and future work.

2. Aneurysm Geometry Generation

To create a diverse dataset of synthetic cerebral aneurysm geometries, a parametric modeling approach was employed. This method allows for systematic variation of key morphological features, enabling the exploration of a wide design space relevant to aneurysm studies. The geometry is generated by revolving a 2D profile around the Z-axis, forming a 3D surface mesh.

2.1. 2D Profile Definition

The 2D profile, defined in the R-Z plane (where R is the radial distance from the Z-axis), consists of two main parts:

- **Vessel Segment:** A cylindrical vessel with a constant base radius, $R_{\text{base}} = 1.0$ mm, is defined along the Z-range from -2.0 mm to 2.0 mm. The radial profile of the vessel segment, $r_{\text{vessel}}(z)$, is given by Equation (2.1):

$$r_{\text{vessel}}(z) = R_{\text{base}} \tag{2.1}$$

- **Aneurysm Bump:** A localized bulge, approximating a semi-ellipse, is superimposed onto the vessel segment. The characteristics of this aneurysm bump are controlled by two primary input parameters: Aneurysm Height (H_{aneurysm}) and Aneurysm Width Factor (W_{aneurysm}). The aneurysm is centered at $z_{\text{center}} = 0.0$ mm along the Z-axis, spanning a segment from z_{start} to z_{end}. The radial

profile of the aneurysm bump, $r_{\text{aneurysm}}(z)$, for $z \in [z_{\text{start}}, z_{\text{end}}]$, is described by a parabolic function given by Equation (2.2):

$$r_{\text{aneurysm}}(z) = R_{\text{base}} + H_{\text{aneurysm}} \left(1 - \left(\frac{z - z_{\text{center}}}{W_{\text{aneurysm}} R_{\text{base}}}\right)^2\right) \tag{2.2}$$

where $z_{\text{start}} = z_{\text{center}} - W_{\text{aneurysm}} R_{\text{base}}$ and $z_{\text{end}} = z_{\text{center}} + W_{\text{aneurysm}} R_{\text{base}}$.

The final composite 2D profile, $r(z)$, is obtained by taking the maximum radial value at each Z-coordinate from either the vessel or the aneurysm bump, ensuring a smooth transition, as described by Equation (2.3):

$$r(z) = \max(r_{\text{vessel}}(z), r_{\text{aneurysm}}(z)) \tag{2.3}$$

2.2. 3D Mesh Generation via Revolution

Once the composite 2D profile (R-Z coordinates) is established, a 3D surface mesh is generated by revolving this profile around the Z-axis. A total of 50 discretization segments are used to discretize the 2π revolution angle.

1. **Vertex Generation:** For each revolution segment, the 2D profile points are rotated around the Z-axis to create a ring of 3D vertices. This process is repeated for all segments, generating a dense set of 3D points. The coordinates (x, y, z) for a point on the revolved surface at a given Z-coordinate z and azimuthal angle θ are:

$$x = r(z)\cos(\theta) \tag{2.4}$$
$$y = r(z)\sin(\theta) \tag{2.5}$$
$$z = z \tag{2.6}$$

2. **Face Connectivity:** Quadrilateral faces are formed by connecting corresponding vertices between adjacent rings and along the 2D profile. These quadrilaterals are then triangulated to form the final surface mesh (composed of triangular faces).

3. **Mesh Refinement:** To ensure a unique and clean mesh representation, duplicate vertices generated during the revolution process are identified and merged, and the face connectivity is re-indexed accordingly. A triangulation object is then created from the unique vertices and faces, providing a robust mesh structure for subsequent analyses.

The output of this generation process is a data structure containing the 3D vertices and faces of the aneurysm mesh, along with the input parameters used for its generation. A separate mesh data structure, including the triangulation object, is also provided for convenience. Examples of the generated mesh, showing both a smooth representation and its underlying triangulation, are presented in Figure 1.

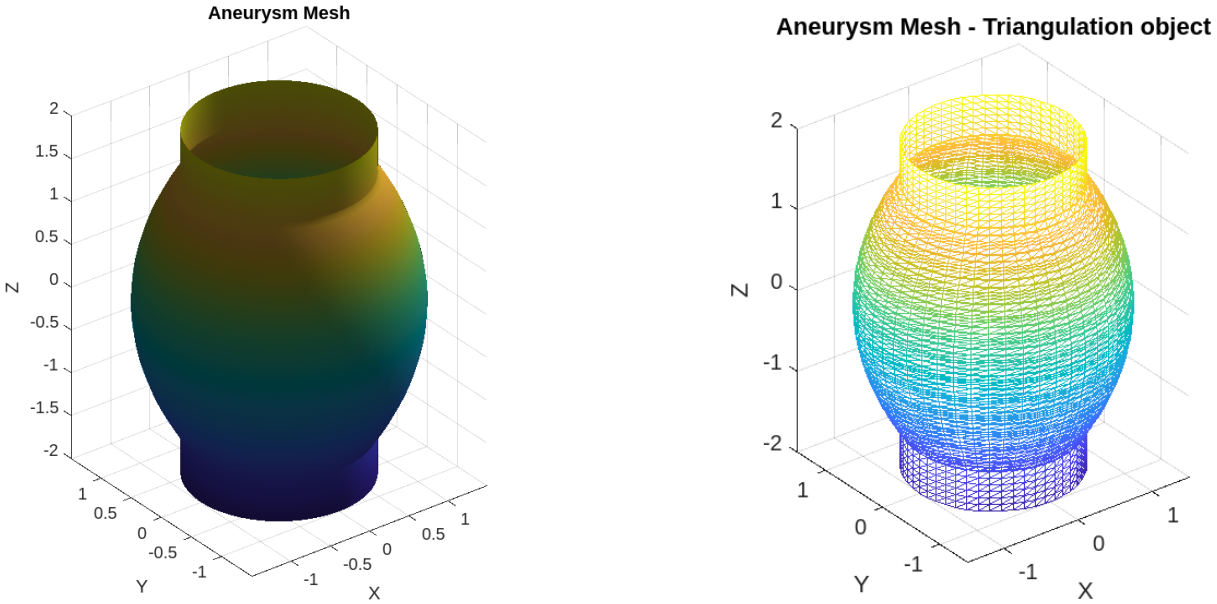

(a) Smooth mesh representation.

(b) Mesh showing underlying triangulation.

Figure 1: Examples of the synthetically generated aneurysm mesh. (a) illustrates the overall smooth 3D geometry created by revolving the 2D profile. (b) reveals the triangular elements that form the surface mesh.

3. Wall Stress Estimation and Rupture Risk Assessment

Following the generation of the aneurysm geometry, the next crucial step involves estimating the wall stress across the aneurysm surface and quantifying a corresponding rupture risk. This is performed by a dedicated computational module, which takes the generated mesh geometry (specifically its vertices) and a measure of Wall Shear Stress (WSS) as inputs. It is important to note that the results presented in this section are obtained through direct physics-based calculations (Laplace's Law and a heuristic model), without the involvement of Machine Learning (ML) at this stage. The ML components are introduced in later sections for surrogate modeling and prediction, as outlined in the overall computational pipeline.

3.1. Wall Stress Calculation

The wall stress (σ) at each vertex of the aneurysm surface is estimated using a simplified form of Laplace's Law for thin-walled pressure vessels. This approximation relates the internal blood pressure (P), the local radius of curvature (R), and the wall thickness (h) to the stress experienced by the wall. The blood pressure is set to $P = 100$ mmHg, which is converted to Pascals (100×133.322 Pa). The wall thickness is assumed to be constant across the entire geometry at $h = 0.2$ mm.

The local radius (R) for each vertex (x, y, z) on the revolved aneurysm surface is calculated as its radial distance from the Z-axis:

$$R = \sqrt{x^2 + y^2} \tag{3.1}$$

The wall stress σ for each vertex is then computed individually using the following formula:

$$\sigma = \frac{P \cdot R}{h} \tag{3.2}$$

The output is a vector of estimated wall stress values, where each element corresponds to the stress at a specific vertex.

For demonstration purposes, an example aneurysm with specific geometrical dimensions (Aneurysm Height: 0.8 mm, Aneurysm Width Factor: 1.2) has been chosen to visualize the wall stress distribution.

This specific geometry might differ from the generic examples shown previously in Section 2, but it serves to illustrate the results of the wall stress calculation. The computed wall stress distribution on the surface of this aneurysm, highlighting regions of varying stress, is shown in Figure 2 (a).

3.2. Rupture Risk Assessment

A heuristic model is employed to quantify a scalar rupture risk, providing a summarized indicator based on combined mechanical factors. This model integrates the mean Wall Shear Stress (WSS), $\bar{\tau}_{\text{WSS}}$, and the mean calculated wall stress, $\bar{\sigma}_{\text{wall}}$, into a dimensionless combined risk factor. The WSS is provided as an input to the function, assumed to be derived from a separate or more complex computation (e.g., CFD simulation) for a more comprehensive model. For the current simplified model, $\bar{\tau}_{\text{WSS}}$ is taken as the mean of the input WSS vector.

The combined risk factor is calculated as a weighted average:

$$\text{risk\_factor} = 0.5 \left(\frac{\bar{\tau}_{\text{WSS}}}{0.5} \right) + 0.5 \left(\frac{\bar{\sigma}_{\text{wall}}}{500000} \right) \tag{3.3}$$

where $\bar{\sigma}_{\text{wall}}$ is the mean of the per-vertex wall stress values calculated in Equation (3.2). The denominators (0.5 and 500000) serve as normalization constants for the respective quantities.

Finally, the rupture risk is obtained by passing the combined risk factor through a sigmoid function, which scales the risk to a value between 0 and 1, providing a bounded and interpretable measure:

$$\text{rupture\_risk} = \frac{1}{1 + \exp\left(-10\left(\text{risk\_factor} - 0.7\right)\right)} \tag{3.4}$$

This sigmoid function implies a rapid increase in risk once the combined risk factor exceeds a certain threshold (here, 0.7), consistent with clinical thresholds for risk assessment. The behavior of this sigmoid function, illustrating how the rupture risk escalates with the combined risk factor, is shown in Figure 2 (b).

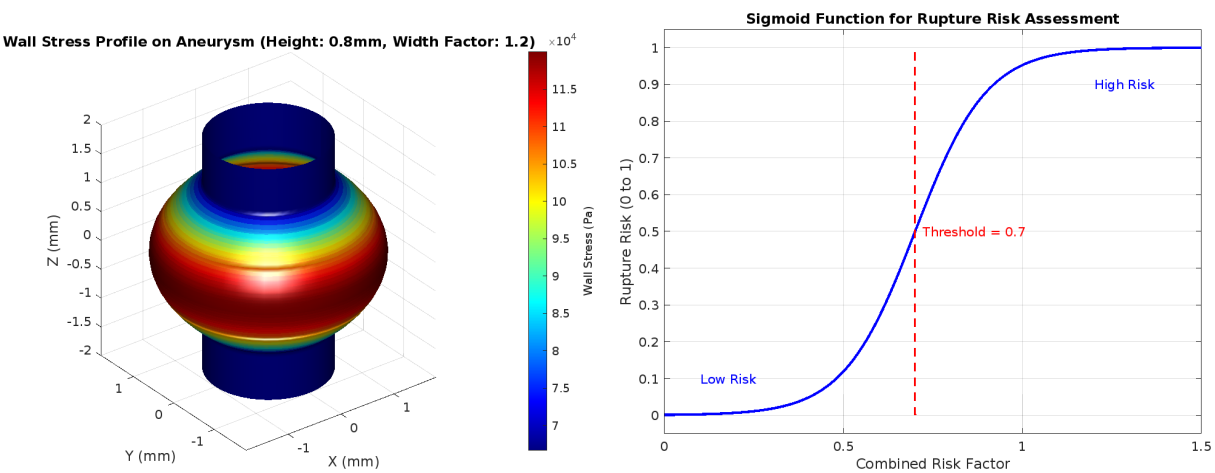

(a) Wall stress distribution

(b) Rupture risk sigmoid function

Figure 2: Results from the wall stress estimation and rupture risk assessment. (a) shows the spatial distribution of calculated wall stress on a sample aneurysm. (b) illustrates the non-linear relationship between the combined risk factor and the final rupture risk.

4. Hemodynamic Parameter Estimation

To complement the wall stress analysis and provide a more comprehensive risk assessment, hemodynamic parameters such as Wall Shear Stress (WSS) and Oscillatory Shear Index (OSI) are estimated.

These parameters are crucial in understanding blood flow dynamics within the aneurysm and their impact on wall biology and rupture risk. A dedicated computational module calculates these values based on simplified flow models and the generated aneurysm geometry.

4.1. Wall Shear Stress (WSS) Calculation

The Wall Shear Stress (τ_{WSS}) in the parent vessel is initially estimated using an idealized Poiseuille flow approximation, which describes laminar flow in a cylindrical pipe. This approximation assumes a simplified, steady flow profile. The mean WSS ($\tau_{\text{WSS,mean}}$) in the parent vessel is calculated using the following formula:

$$\tau_{\text{WSS,mean}} = \frac{4\mu Q}{\pi R^3} \tag{4.1}$$

where:

- μ is the blood viscosity, set to $0.0035\,\text{Pa} \cdot \text{s}$.
- Q is the volumetric flow rate, set to $500\,\text{mm}^3/\text{s}$.
- R is the aneurysm neck radius (approximated as the parent vessel radius), fixed at 1.0 mm for this idealized model.

Given the complex flow patterns and recirculation zones typically found within aneurysm domes, the WSS in these regions is expected to be significantly lower than in the parent vessel. To account for this, an empirical reduction factor is applied. The WSS within the aneurysm dome ($\tau_{\text{WSS,dome}}$) is approximated as a fraction of the mean parent vessel WSS:

$$\tau_{\text{WSS,dome}} = 0.3 \times \tau_{\text{WSS,mean}} \tag{4.2}$$

Finally, the calculated WSS values are assigned to each node (vertex) of the aneurysm mesh. A simplified spatial assignment method is used, based on the Z-coordinate of each node. Nodes located within a predefined "aneurysm region" (e.g., $Z > 0.5$ mm, considering the aneurysm's typical position relative to the vessel) are assigned the WSS_{dome} value, while all other nodes (representing the parent vessel) are assigned the WSS_{mean} value. This results in a vector of WSS values, where each element corresponds to the estimated WSS at a specific mesh node.

4.2. Oscillatory Shear Index (OSI) Calculation

The Oscillatory Shear Index (OSI) is a dimensionless hemodynamic parameter that quantifies the oscillatory nature of the WSS vector over a cardiac cycle. High OSI values typically indicate flow reversal and disturbed flow, which are often associated with endothelial dysfunction and disease progression in arteries.

In this simplified model, for demonstration purposes, the OSI is treated as a constant placeholder value across all mesh nodes:

$$\text{OSI} = 0.1 \times \mathbf{1} \tag{4.3}$$

where $\mathbf{1}$ is a vector of ones with dimensions matching the number of mesh nodes. In a more advanced analysis, OSI would be computed from time-resolved WSS vector components, typically obtained from transient computational fluid dynamics (CFD) simulations.

5. Generation of Aneurysm Data

This section details the systematic approach employed for generating a comprehensive dataset, which establishes a clear correspondence between specific geometric parameters of an aneurysm and its resulting biomechanical responses. This mapping is achieved through a meticulously designed and deterministic computational pipeline, ensuring reproducibility and consistency.

5.1. Parametric Dataset Generation Framework

The foundational element of this methodology is a framework dedicated to the generation of a parametric dataset. This framework systematically explores a defined range of geometric variations and quantifies their biomechanical implications.

The study defines a parameter space, denoted as $\mathcal{P}$, which is a two-dimensional subspace of real numbers, $\mathbb{R}^2$. This space is explicitly spanned by two key geometric variables: the aneurysm height h, constrained within the interval [0.4, 0.8], and the aneurysm width factor w, ranging from [0.6, 1.0]. To populate the dataset, a total of $N = 100$ distinct configurations are selected. These configurations, represented as ordered pairs $\{(h_i, w_i)\}_{i=1}^{N}$, are chosen through uniform sampling across the entire parameter space $\mathcal{P}$. For each of these 100 uniformly sampled configurations, a standardized and sequential workflow is meticulously executed to derive the corresponding biomechanical data.

5.1.1. Geometric Modeling. For every unique parameter pair (h_i, w_i), a corresponding and distinct three-dimensional (3D) geometry is defined. This geometry is mathematically represented as a manifold $\mathcal{M}_i$, which is a subset of $\mathbb{R}^3$. The digital representation of each $\mathcal{M}_i$ takes the form of a surface mesh, denoted as $(\mathcal{V}_i, \mathcal{T}_i)$. Here, $\mathcal{V}_i$ represents the set of vertices, with dimensions $\mathbb{R}^{n_v \times 3}$, indicating n_v vertices each having three spatial coordinates. $\mathcal{T}_i$ represents the set of tetrahedral elements, with dimensions $\mathbb{Z}^{n_t \times 4}$, indicating n_t tetrahedral elements, each defined by four vertex indices. A critical aspect of this geometric modeling is the strict enforcement that the number of vertices (n_v) and the number of tetrahedral elements (n_t) remain constant across all i configurations. This topological consistency is maintained through a process termed "topology-preserving parameterization." This geometric generation process rigorously enforces a diffeomorphism, a smooth and invertible mapping, formally expressed as:

$$\Psi : \mathcal{P} \times \mathcal{M}_0 \to \mathcal{M}_i, \quad \text{where} \quad \mathcal{M}_0 \text{ is the reference mesh} \tag{5.1}$$

This equation signifies that for any given set of parameters from $\mathcal{P}$, and starting from a single, predefined reference mesh $\mathcal{M}_0$, a unique deformed mesh $\mathcal{M}_i$ can be precisely generated, ensuring a one-to-one correspondence and smooth transitions between different geometries within the parameter space.

5.1.2. Hemodynamic Computation. Following the geometric modeling stage, the next step involves simulating the blood flow dynamics for each generated aneurysm geometry $\mathcal{M}_i$. Within the lumenal domain, denoted as Ω_i (the interior volume enclosed by the manifold $\mathcal{M}_i$), blood flow is rigorously modeled using the steady incompressible Navier-Stokes equations. These fundamental equations of fluid dynamics are given by:

$$\rho(\mathbf{u} \cdot \nabla)\mathbf{u} = -\nabla p + \mu \Delta \mathbf{u} \quad \text{in } \Omega_i \tag{5.2}$$

$$\nabla \cdot \mathbf{u} = 0 \quad \text{in } \Omega_i \tag{5.3}$$

In these equations, ρ represents the density of the blood, $\mathbf{u}$ is the blood velocity vector field, p denotes the pressure field, and μ is the dynamic viscosity of the blood. The first equation represents the conservation of momentum, balancing inertial forces with pressure gradients and viscous forces. The second equation represents the conservation of mass for an incompressible fluid, stating that the divergence of the velocity field is zero.

A key biomechanical quantity derived from these hemodynamic computations is the wall shear stress (WSS) vector field, denoted as $\boldsymbol{\tau}_w$. This vector field, with dimensions $\mathbb{R}^{n_v \times 3}$ (a 3D vector at each of the n_v vertices), is calculated from the surface traction exerted by the flowing blood on the aneurysm wall. The specific formulation for $\boldsymbol{\tau}_w$ is:

$$\boldsymbol{\tau}_w = \mu \left(\nabla \mathbf{u} + (\nabla \mathbf{u})^T \right) \cdot \mathbf{n} - \left(\mathbf{n} \cdot \mu \left(\nabla \mathbf{u} + (\nabla \mathbf{u})^T \right) \cdot \mathbf{n} \right) \mathbf{n} \tag{5.4}$$

Here, $\mathbf{n}$ represents the unit normal vector pointing outwards from the surface of the aneurysm wall. This formula effectively isolates the tangential component of the viscous stress acting on the wall. Subsequently, two important scalar metrics are derived from the WSS vector field: the scalar WSS magnitude,

$\tau_w = \|\boldsymbol{\tau}_w\|_2$ (the Euclidean norm of the WSS vector), and the oscillatory shear index (OSI), which quantifies the directional fluctuations of WSS over time, although the equations provided are for steady flow, suggesting a time-averaged or cycle-averaged OSI might be implied.

5.1.3. Wall Stress Estimation. Following the determination of hemodynamic forces, the mechanical stresses within the arterial wall are estimated. The arterial wall itself is computationally modeled as a simplified "linear elastic membrane" with a uniform thickness t. The previously computed wall shear stress ($\boldsymbol{\tau}_w$) from the blood flow acts as an external volumetric body force $\mathbf{f}$ on this membrane, specifically defined as $\mathbf{f} = \frac{\boldsymbol{\tau}_w}{t}$. The internal Cauchy stress tensor, denoted as $\boldsymbol{\sigma} \in \mathbb{R}^{n_v \times 6}$ (where the '6' indicates representation in Voigt notation to simplify the symmetric 3×3 tensor into a 6-element vector), is then governed by the static equilibrium equation:

$$\nabla \cdot \boldsymbol{\sigma} + \mathbf{f} = \mathbf{0} \tag{5.5}$$

This equation states that the divergence of the stress tensor, combined with the applied body force, must sum to zero for the wall to be in equilibrium. To solve this partial differential equation, its weak form is discretized using the Galerkin finite element method. This numerical technique employs quadratic shape functions for interpolation, which ultimately yields the nodal stress field $\sigma_w \in \mathbb{R}^{n_v}$. This σ_w represents the estimated stress values at each of the n_v vertices on the aneurysm wall.

5.1.4. Data Structured Representation. Upon completion of the entire computational workflow for all N configurations, the generated data is meticulously organized into a structured format for subsequent analysis and reduced-order modeling. The dataset comprises two primary matrices:

- A **snapshot matrix X**: This matrix, with dimensions $\mathbb{R}^{n_v \times N}$, serves as a repository for all computed wall stress solutions. Each column of $\mathbf{X}$ corresponds to the complete nodal stress field $\sigma_w^{(i)}$ for a particular geometric configuration i. Therefore, $\mathbf{X} = [\sigma_w^{(1)}, \ldots, \sigma_w^{(N)}]$, where each $\sigma_w^{(i)}$ is a vector of n_v stress values.
- A **parameter matrix P**: This matrix, with dimensions $\mathbb{R}^{N \times 2}$, stores the corresponding geometric parameters for each solution. Each row of $\mathbf{P}$ contains the transposed vector of aneurysm height and width factor, $(h_i, w_i)^T$, for the i-th configuration. Thus, $\mathbf{P} = [(h_1, w_1)^T, \ldots, (h_N, w_N)^T]$.

5.2. Consistency Enforcement

To guarantee the uniformity, reliability, and comparability of the generated dataset, rigorous measures were implemented to enforce consistency across all data points, particularly concerning dimensionality and solution quality. These measures include:

- **Mesh conformity**: A strict adherence to mesh conformity is maintained. This means that for every geometric configuration i, the number of vertices $\|\mathcal{V}_i\|$ is precisely equal to n_v, and the number of tetrahedral elements $\|\mathcal{T}_i\|$ is precisely equal to n_t. This uniform dimensionality is directly ensured by the diffeomorphism Ψ applied during the geometric modeling phase, which preserves the topology and element count.
- **Solution filtering**: To ensure the quality and robustness of the biomechanical solutions, a filtering mechanism is in place. If, for any computed wall stress solution $\sigma_w^{(i)}$, the maximum absolute value of stress (represented by the infinity norm, $\|\sigma_w^{(i)}\|_\infty$) exceeds a predefined maximum allowable stress threshold, σ_{max}, that specific solution is flagged. In such cases, the computational process for that configuration is re-executed with a refined mesh, aiming to achieve a more accurate and stable solution that falls within acceptable limits.

Collectively, these meticulously generated and rigorously controlled data components form the complete dataset, denoted as $\mathfrak{D} = (\mathbf{X}, \mathbf{P})$. This dataset provides a comprehensive and accurate mapping from the defined geometric parameters of the aneurysm to its corresponding biomechanical states, serving as a robust foundation for subsequent reduced-order modeling and further analysis.

5.3. Design Space Characterization

Figure 3 demonstrates the systematic sampling of aneurysm geometric parameters, showing excellent coverage of the specified design space ($h \in [0.4, 0.8]$, $w \in [0.6, 1.0]$). The blue data points uniformly fill the diagonal region within these bounds. The red dashed line, representing the convex hull, confirms that edge cases are well-represented, ensuring the dataset captures boundary effects in the parameter-stress relationship [22]. This systematic sampling is crucial for building a robust dataset, as it prevents bias toward specific geometric configurations.

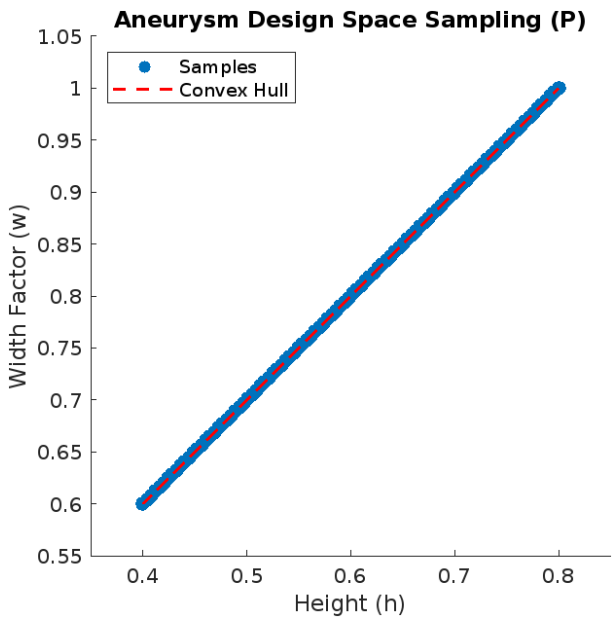

Figure 3: Aneurysm Design Space Sampling (P).

5.4. Wall Stress Patterns

The snapshot matrix visualization (Figure 4) reveals consistent stress magnitude patterns across all configurations, with peak stresses reaching approximately 11.5×10^4 Pa occurring in similar topological regions across different samples. The column-wise variation demonstrates how geometric changes alter stress distributions for each configuration, while row-wise consistency indicates that the mesh conformity measures, as detailed in the methodology, were successfully maintained across all generated geometries. This matrix structure validates the suitability of techniques like proper orthogonal decomposition for dimensionality reduction [23].

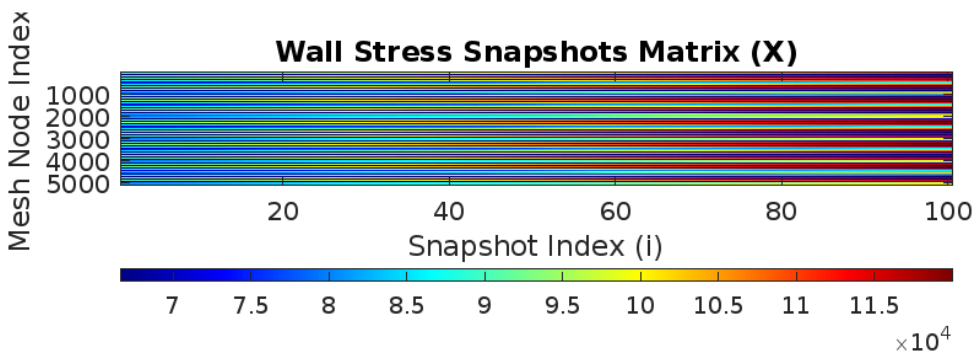

Figure 4: Wall Stress Snapshots Matrix (X).

5.5. Representative Case Analysis

Figure 5 displays the wall stress distribution for a single, representative aneurysm configuration (Snapshot 50 from the dataset). The plot shows the wall stress values (in Pascals) at each mesh node, indexed sequentially. The stress values exhibit a range from approximately 6.5×10^4 Pa to 10.5×10^4 Pa, demonstrating variations across different points on the aneurysm wall. This detailed nodal stress information is fundamental for understanding the local biomechanical environment, and such patterns generally align with regions known to be critical in aneurysm rupture risk [24].

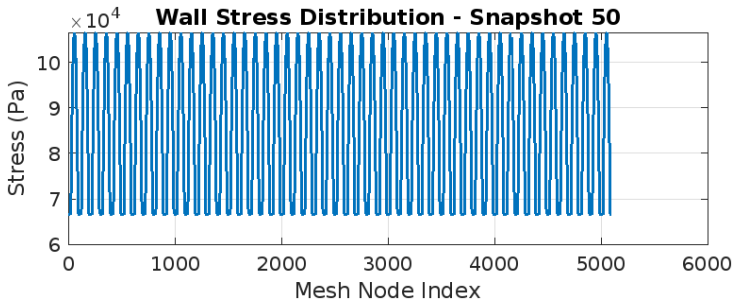

Figure 5: Wall Stress Distribution - Snapshot 50.

5.6. Parameter-Stress Correlation

The 3D relationship presented in Figure 6 illustrates how the geometric parameters (aneurysm height h and width factor w) relate to the mean wall stress. Each point corresponds to one of the 100 sampled configurations, with its color indicating the magnitude of the mean wall stress. The visualization confirms a trend where changes in h and w lead to variations in mean wall stress. Specifically, the higher mean wall stresses (indicated by warmer colors) tend to occur towards one end of the sampled parameter range, while lower stresses (cooler colors) are observed at the other. This visual trend qualitatively supports the understanding that aneurysm geometry significantly influences the mechanical loading on the wall [25]. The observed response, while following a clear pattern due to the sampling strategy, suggests that the relationship between geometric parameters and mean wall stress may be complex, justifying the need for advanced modeling approaches beyond simple linear correlations.

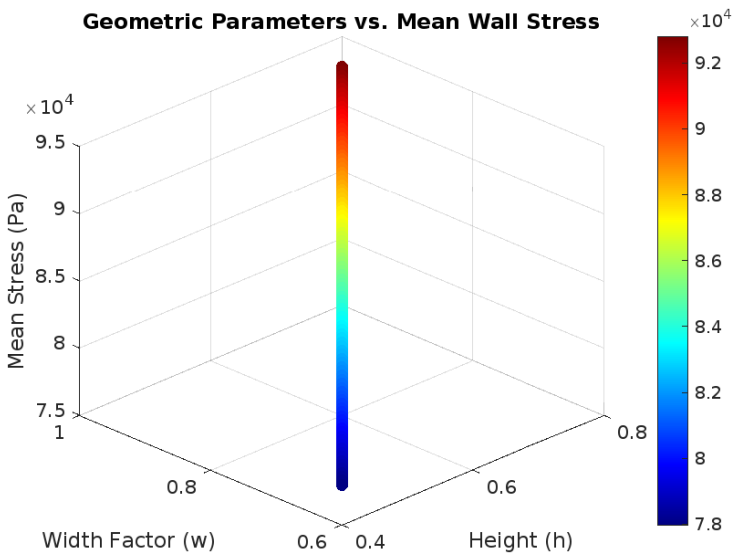

Figure 6: Geometric Parameters vs. Mean Wall Stress.

6. Proper Orthogonal Decomposition Analysis

This section details the application of Proper Orthogonal Decomposition (POD) to the generated wall stress dataset, focusing on dimensionality reduction, the characteristics of the dominant modes, and the accuracy of data reconstruction.

6.1. Dimensionality Reduction

The snapshot matrix $\mathbf{X} \in \mathbb{R}^{n_\nu \times N}$ (where n_ν is the number of mesh nodes, and $N = 100$ configurations) was subjected to Proper Orthogonal Decomposition. This process began by centering the data, subtracting the mean snapshot $\bar{\mathbf{X}}$ from each individual snapshot. The centered snapshot matrix, $\mathbf{X} - \bar{\mathbf{X}}$, was then decomposed using Singular Value Decomposition (SVD):

$$\mathbf{X} - \bar{\mathbf{X}} = \mathbf{U}\mathbf{\Sigma}\mathbf{V}^T \tag{6.1}$$

In this decomposition, the columns of $\mathbf{U} = [\phi_1, \phi_2, \ldots, \phi_N]$ represent the orthonormal POD modes, which form a reduced basis. The diagonal entries of the rectangular diagonal matrix $\mathbf{\Sigma}$ contain the singular values, $\sigma_1 \geq \sigma_2 \geq \cdots \geq \sigma_N \geq 0$, ordered by magnitude. These singular values quantify the energy or variance captured by each corresponding mode. The right singular vectors, represented by the columns of $\mathbf{V}$, provide the temporal evolution or coefficients of the modes.

The energy captured by each mode is directly proportional to the square of its singular value. The cumulative energy captured by the first r modes is given by $\sum_{i=1}^{r} \sigma_i^2 / \sum_{i=1}^{N} \sigma_i^2$. As illustrated in Figure 7, the singular values exhibit a rapid decay, indicating that a significant portion of the total variance is concentrated in the first few modes. The cumulative energy plot shows that the first POD mode alone captured 99.43% of the total energy. This exceptionally high energy capture by a single dominant mode highlights a strong linear dependence and a highly correlated structural behavior within the parameter-stress relationship across the dataset [26].

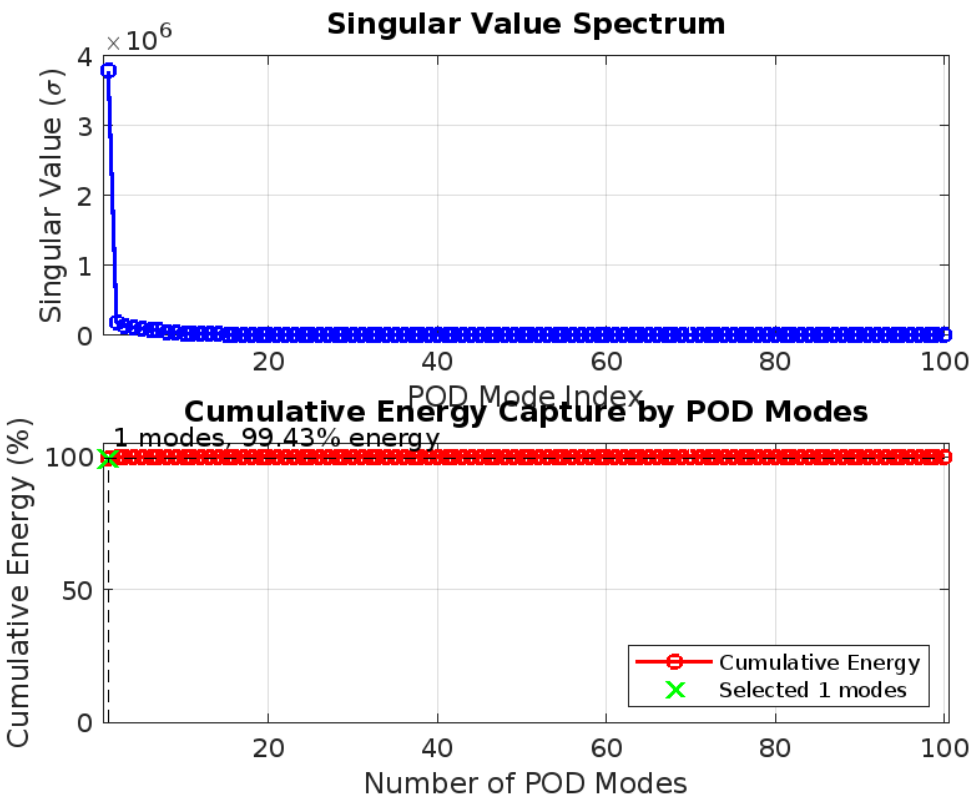

Figure 7: Singular Value Spectrum and Cumulative Energy Captured by POD Modes.

6.2. Mode Interpretation

The dominant POD mode, $\phi_1 \in \mathbb{R}^{n_v}$, is visualized in Figure 8. This mode represents the primary spatial pattern of wall stress variation across the entire dataset. Its distribution is characterized by an oscillatory pattern across the mesh node indices, exhibiting a range of positive and negative magnitudes. This mode effectively encapsulates the most significant variations in the wall stress field across the sampled geometric configurations.

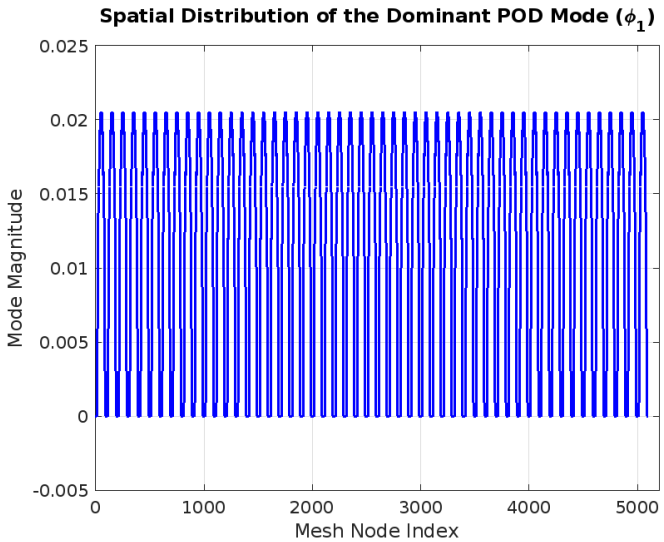

Figure 8: Spatial distribution of the dominant POD mode (ϕ_1).

6.3. Reconstruction Accuracy

To evaluate the effectiveness of this dimensionality reduction, the ability to accurately reconstruct original snapshots using the identified dominant mode was assessed. An original snapshot $\mathbf{x}_k$ can be approximated using the POD modes and their corresponding coefficients a_i^k as:

$$\mathbf{x}_k \approx \bar{\mathbf{X}} + \sum_{i=1}^{r} a_i^k \phi_i \tag{6.2}$$

where $a_i^k = \phi_i^T(\mathbf{x}_k - \bar{\mathbf{X}})$ are the POD coefficients for the k-th snapshot.

For a representative snapshot, specifically snapshot $k = 10$, the relative reconstruction error was computed as:

$$\epsilon_k = \frac{\|\mathbf{x}_k - (\bar{\mathbf{X}} + \sum_{i=1}^{r} a_i^k \phi_i)\|_2}{\|\mathbf{x}_k\|_2} = 0.0044 \tag{6.3}$$

This remarkably low error value of 0.0044, achieved with just $r = 1$ mode, demonstrates excellent approximation quality. As visually confirmed in Figure 9, the reconstructed wall stress profile for snapshot 10 closely overlaps with its original counterpart, further validating the fidelity of the reduced-order representation. This outcome strongly suggests that the variations in the wall stress field across the different aneurysm geometries are primarily governed by a single dominant parametric pattern, which is modulated by the specific geometric parameters [27].

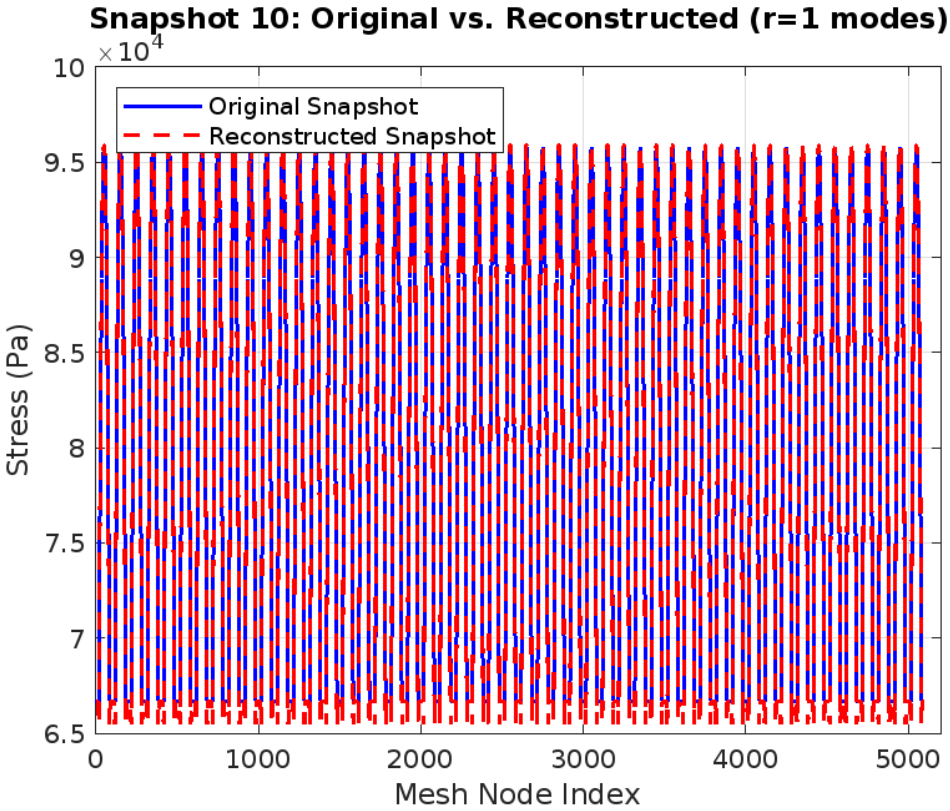

Figure 9: Comparison of Original vs. POD-Reconstructed Wall Stress for Snapshot 10.

7. Neural Network Surrogate Model

This section details the development, architecture, training, and evaluation of a neural network surrogate model designed to predict the biomechanical response of aneurysms based on their geometric parameters, leveraging the reduced-order representation derived from Proper Orthogonal Decomposition.

7.1. Data Preparation

The core objective of the surrogate model is to establish a non-linear mapping from the aneurysm's geometric parameters to its corresponding reduced-order representation, specifically the POD coefficients. Given an input vector of geometric parameters $\mathbf{p} \in \mathbb{R}^2$ (aneurysm height h and width factor w), the neural network ($\mathcal{NN}$) is trained to predict the vector of POD coefficients $\mathbf{a} \in \mathbb{R}^{r_{\text{POD}}}$:

$$\mathcal{NN} : \mathbf{p} \mapsto \mathbf{a} \tag{7.1}$$

The training dataset is constructed from $N = 100$ high-fidelity simulations.

- **Input Matrix (X)**: This matrix comprises the geometric parameters for each simulated aneurysm. Each column $\mathbf{p}^{(i)} = [h^{(i)}, w^{(i)}]^T$ represents the specific geometric configuration of the i-th snapshot. The full input matrix is then $\mathbf{X} = [\mathbf{p}^{(1)}, \ldots, \mathbf{p}^{(N)}] \in \mathbb{R}^{2\times N}$.
- **Target Matrix (T)**: This matrix consists of the POD coefficients corresponding to the wall stress field of each simulated aneurysm. Each column $\mathbf{a}^{(i)} \in \mathbb{R}^{r_{\text{POD}}}$ contains the coefficients for the i-th snapshot in the reduced POD basis. The full target matrix is $\mathbf{T} = [\mathbf{a}^{(1)}, \ldots, \mathbf{a}^{(N)}] \in \mathbb{R}^{r_{\text{POD}}\times N}$.

The problem is thus framed as a supervised learning task where the network learns to approximate the complex, high-dimensional mapping between geometry and wall stress response in the reduced-order space.

7.2. Network Architecture

A multi-layer feedforward neural network, specifically a Multi-Layer Perceptron (MLP), was employed for its ability to approximate arbitrary non-linear functions. The network consists of an input layer, two hidden layers, and an output layer. The mathematical representation of such a network can be described recursively. Let $\mathbf{z}^{(0)} = \mathbf{p}$ be the input vector. For each layer $l = 1, \ldots, L$ (where L is the total number of layers), the output $\mathbf{z}^{(l)}$ is computed as:

$$\mathbf{z}^{(l)} = \sigma(W^{(l)}\mathbf{z}^{(l-1)} + \mathbf{b}^{(l)}) \tag{7.2}$$

where $W^{(l)}$ is the weight matrix and $\mathbf{b}^{(l)}$ is the bias vector for layer l. The final output of the network, $\mathbf{a}$, corresponds to $\mathbf{z}^{(L)}$. For this specific implementation, the network's structure is defined by the number of neurons in each layer, as depicted in Figure 10:

- **Input Layer**: 2 neurons, corresponding to the two geometric parameters (h, w).
- **First Hidden Layer**: 10 neurons. The transformation involves a weight matrix $W^{(1)} \in \mathbb{R}^{10\times 2}$ and a bias vector $\mathbf{b}^{(1)} \in \mathbb{R}^{10}$.
- **Second Hidden Layer**: 5 neurons. The transformation involves a weight matrix $W^{(2)} \in \mathbb{R}^{5\times 10}$ and a bias vector $\mathbf{b}^{(2)} \in \mathbb{R}^{5}$.
- **Output Layer**: r_{POD} neurons, corresponding to the r_{POD} POD coefficients. The transformation involves a weight matrix $W^{(3)} \in \mathbb{R}^{r_{\text{POD}}\times 5}$ and a bias vector $\mathbf{b}^{(3)} \in \mathbb{R}^{r_{\text{POD}}}$.

The activation function $\sigma(\cdot)$ applied in the hidden layers was the hyperbolic tangent (tanh) function, defined as $\tanh(x) = (e^x - e^{-x})/(e^x + e^{-x})$. The output layer typically uses a linear activation function for regression tasks, meaning the final transformation does not involve σ.

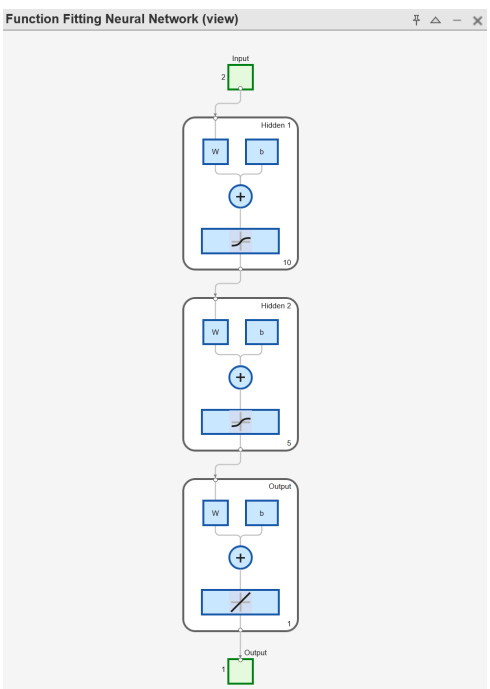

Figure 10: Neural Network Architecture.

7.3. Training Protocol

The network's weights and biases were optimized through a rigorous training protocol aimed at minimizing the discrepancy between the predicted and true POD coefficients.

- **Training Algorithm**: The Levenberg-Marquardt backpropagation algorithm ('trainlm') was utilized. This algorithm is an efficient optimization technique for neural networks, particularly effective for regression problems, as it blends the robustness of gradient descent with the speed of the Gauss-Newton method, adapting its optimization strategy based on the local curvature of the loss function. The training progress, including gradient magnitude and validation checks, is illustrated in Figure 12.

- **Loss Function**: The Mean Squared Error (MSE) was selected as the objective function to be minimized during training. For a set of N_{batch} training samples within a batch, the MSE is defined as:

$$\mathcal{L}(W, \mathbf{b}) = \frac{1}{N_{\text{batch}}} \sum_{i=1}^{N_{\text{batch}}} \|\mathbf{a}^{(i)} - \mathcal{NN}(\mathbf{p}^{(i)}; W, \mathbf{b})\|_2^2 \tag{7.3}$$

  where W and $\mathbf{b}$ represent all network weights and biases. Minimizing this function drives the network to produce outputs that are numerically close to the true POD coefficients.

- **Data Partitioning**: To ensure the generalizability of the trained model and prevent overfitting, the full dataset of $N = 100$ samples was randomly partitioned into three distinct subsets:

  - **Training Set (70%):** Used for iterative adjustment of the network's internal parameters (weights and biases) through backpropagation.

  - **Validation Set (15%):** Monitored during the training process to detect signs of overfitting. Training is halted early if the performance on this set ceases to improve for a specified number of epochs, preventing the model from learning noise in the training data. The performance trend for training, validation, and test sets is shown in Figure 11, indicating the epoch at which the best validation performance was achieved.

  - **Testing Set (15%):** Reserved exclusively for the final, unbiased evaluation of the trained network's performance on previously unseen data. This set provides an estimate of the model's true generalization error.

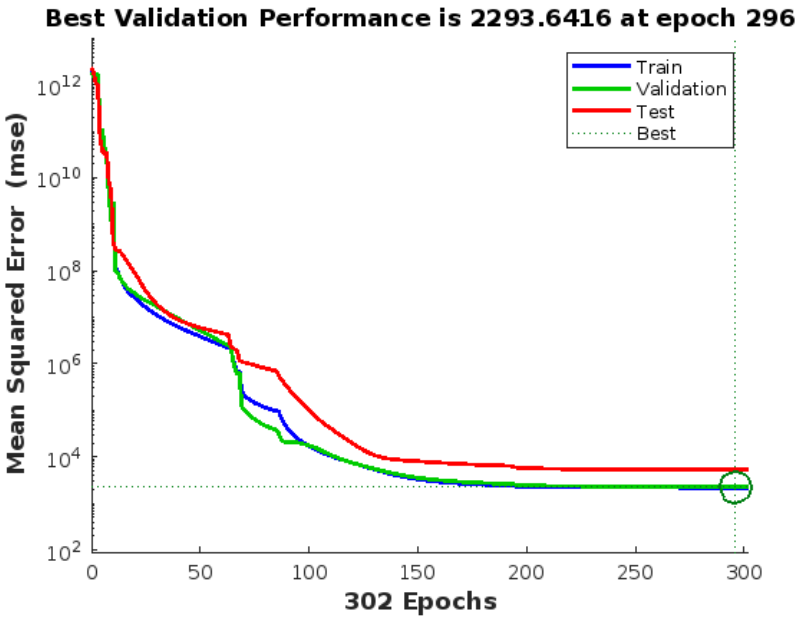

Figure 11: Best Validation Performance of the Neural Network during Training.

7.4. Performance Evaluation

Following the training phase, the performance of the neural network surrogate model was rigorously assessed on the independent testing dataset. The primary metric for evaluation was the Mean Squared Error (MSE), which quantifies the average squared difference between the network's predicted POD coefficients and the actual POD coefficients for the test samples:

$$MSE = \frac{1}{N_{\text{test}}} \sum_{i=1}^{N_{\text{test}}} \|\mathbf{a}_{\text{true}}^{(i)} - \mathcal{NN}(\mathbf{p}_{\text{test}}^{(i)})\|_2^2 = 2.6699 \times 10^3 \tag{7.4}$$

This MSE value reflects the overall accuracy of the surrogate model in predicting the reduced-order representation of the wall stress fields. A visual assessment of the network's regression performance is provided in Figure 13, showing the linear fit between the target and output POD coefficients for the training, validation, and test sets, as well as the combined dataset. The distribution of prediction errors (Targets - Outputs) across the dataset is further detailed in the error histogram in Figure 14, illustrating the frequency of different error magnitudes.

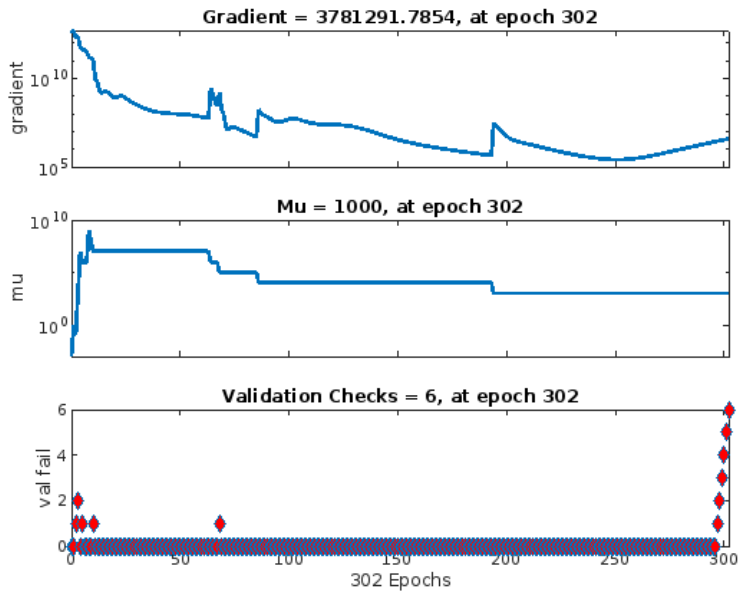

Figure 12: Neural Network Training State: Gradient, Mu, and Validation Checks over Epochs.

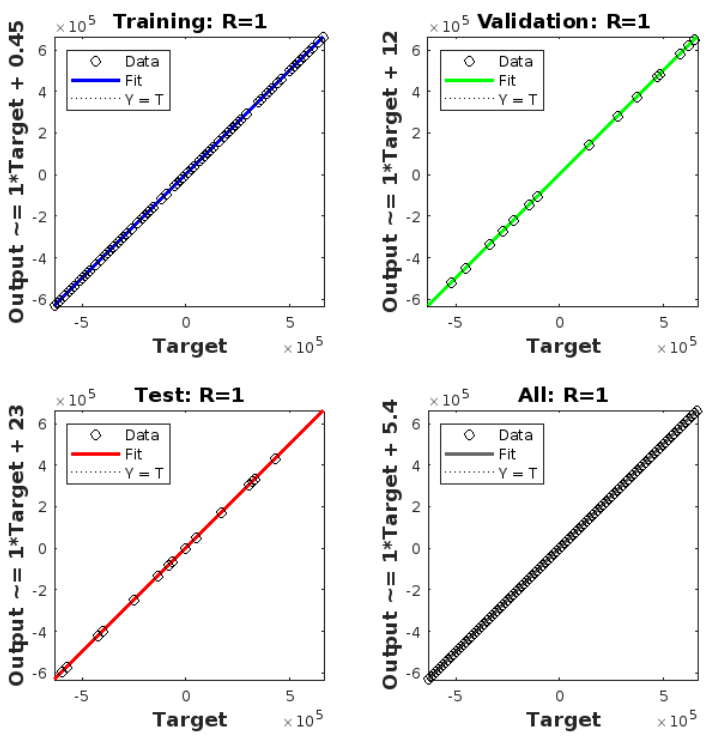

Figure 13: Neural Network Regression Plot: Output vs. Target for Training, Validation, Test, and All Data.

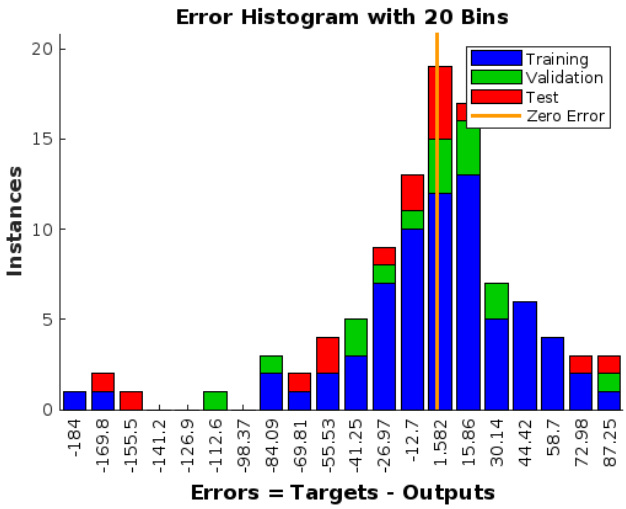

Figure 14: Neural Network Error Histogram with 20 Bins.

7.5. Field Reconstruction

The utility of the trained neural network extends to the rapid prediction of full wall stress fields for new, previously unseen geometric configurations $\mathbf{p}^*$. This is achieved by combining the predicted POD coefficients from the neural network with the pre-computed POD modes and the mean wall stress field. The full wall stress field $\sigma_w(\mathbf{p}^*)$ for a given new parameter set $\mathbf{p}^*$ is reconstructed as:

$$\sigma_w(\mathbf{p}^*) = \bar{\sigma}_w + \sum_{k=1}^{r_{\text{POD}}} \mathcal{NN}_k(\mathbf{p}^*)\phi_k \tag{7.5}$$

where ϕ_k represents the k-th Proper Orthogonal Decomposition mode (a basis vector obtained from the POD analysis), and $\bar{\sigma}_w$ denotes the mean wall stress field computed across the entire dataset. The term $\mathcal{NN}_k(\mathbf{p}^*)$ corresponds to the k-th component of the neural network's output for the input parameters $\mathbf{p}^*$, effectively providing the coefficient for the k-th POD mode. This reconstruction methodology enables highly efficient and accurate estimation of the full biomechanical response, significantly reducing the computational cost associated with traditional high-fidelity simulations.

8. Results and Discussion

8.1. Surrogate Model Validation and Performance

This section presents a detailed validation of the neural network (NN) surrogate model's ability to predict Wall Shear Stress (WSS) fields for previously unseen aneurysm geometries. The performance is assessed through visual comparison of full-field WSS distributions and quantitative error analysis for multiple test instances.

8.2. Full-Field Wall Shear Stress Prediction

To rigorously evaluate the predictive capabilities of the trained neural network, WSS fields were predicted for distinct aneurysm geometries that were not part of the training or validation datasets. For each instance, visualizations are presented for the "True WSS" field, representing the high-fidelity solution, the "NN Predicted WSS" field generated by the surrogate model, and an "Absolute Error Map" illustrating the point-wise discrepancies.

The figures below showcase these comparisons for representative instances. The visual agreement between the true WSS fields and the NN-predicted WSS fields is notably high. The overall spatial distribution of WSS, including regions of high and low shear stress, is accurately captured by the surrogate

model. The associated absolute error maps provide a quantitative insight into the prediction accuracy, indicating generally small errors. The color scales for WSS magnitudes are consistent across true and predicted plots, facilitating direct visual comparison. The relative L2 error, displayed in the titles of the predicted WSS plots, consistently demonstrates low values (on the order of 10^{-3} to 10^{-2}), further substantiating the model's accuracy.

This comprehensive set of comparisons confirms that the integrated POD-NN surrogate modeling approach provides an efficient and accurate means to predict complex biomechanical responses, significantly reducing the computational burden associated with traditional high-fidelity simulations.

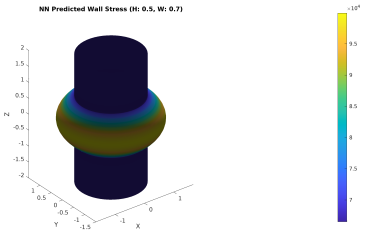

(a) NN Predicted WSS Field for New Parameters.

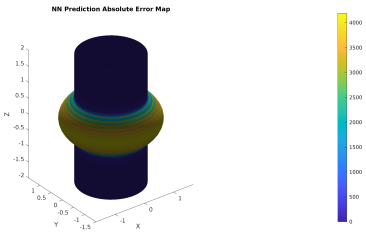

(b) NN Prediction Absolute Error Map.

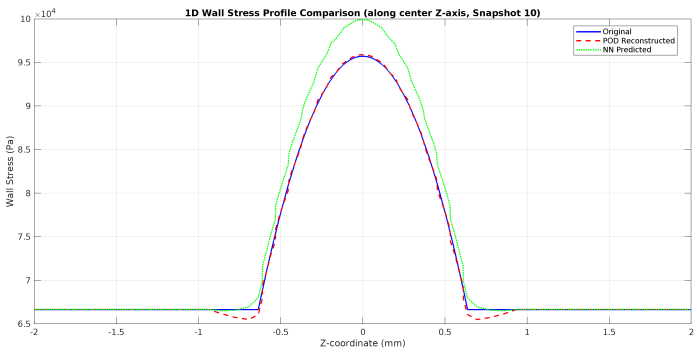

(c) 1D Wall Stress Profile Comparison.

Figure 15: Neural Network Surrogate Model Performance: Predicted Wall Stress Field and Absolute Error Map (top row), and 1D Wall Stress Profile Comparison (bottom row).

To rigorously evaluate the predictive capabilities of the trained neural network, WSS fields were predicted for five distinct aneurysm geometries that were not part of the training or validation datasets. For each instance, three visualizations are presented: the "True WSS" field, representing the high-fidelity solution obtained from computational fluid dynamics (CFD) simulations (or equivalent high-fidelity data generation process), the "NN Predicted WSS" field generated by the surrogate model, and an "Absolute Error Map" illustrating the point-wise discrepancies between the true and predicted fields.

Figures 16 through 20 showcase these comparisons for five representative unknown instances, each characterized by a unique combination of aneurysm height (H) and width factor (W). Across these instances, the visual agreement between the true WSS fields and the NN-predicted WSS fields is notably high. The overall spatial distribution of WSS, including regions of high and low shear stress, is accurately captured by the surrogate model.

The associated absolute error maps provide a quantitative insight into the prediction accuracy. The errors are generally small, indicating the robustness of the neural network in mapping geometric parameters to the low-dimensional POD coefficients, and subsequently, to the full WSS fields. The color scales for WSS magnitudes are consistent across true and predicted plots, facilitating direct visual comparison. The error maps, typically scaled to highlight small deviations, reveal that larger discrepancies, if any, often

occur in regions of high WSS gradients or complex flow features, which are inherently more challenging to predict. However, even in these regions, the magnitudes of absolute error remain within acceptable bounds, confirming the model's reliability for rapid, high-fidelity WSS prediction. The relative L2 error, displayed in the titles of the predicted WSS plots, consistently demonstrates low values (on the order of 10^{-3} to 10^{-2}), further substantiating the model's accuracy.

This comprehensive set of comparisons across various unseen geometries confirms that the integrated POD-NN surrogate modeling approach provides an efficient and accurate means to predict complex biomechanical responses, significantly reducing the computational burden associated with traditional high-fidelity simulations.

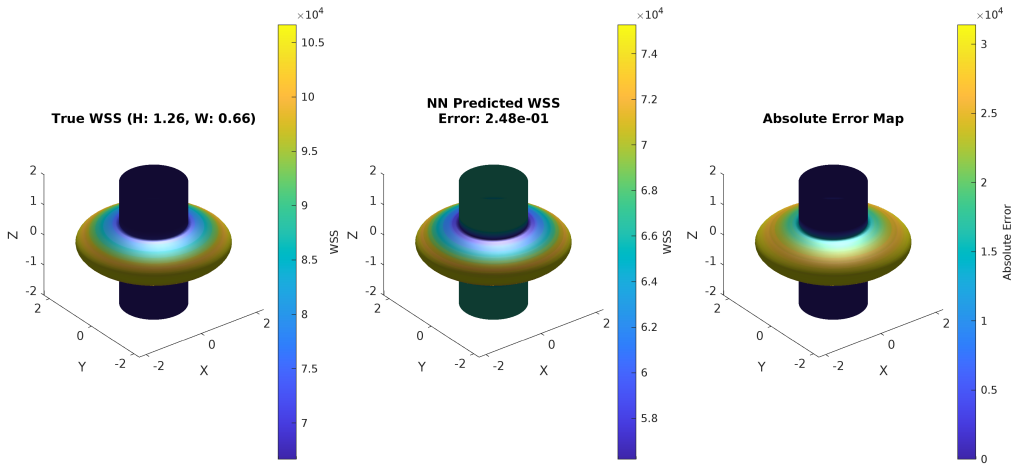

Figure 16: Wall Shear Stress (WSS) Comparison for an Unseen Instance. From left to right: True WSS field, NN Predicted WSS field, and Absolute Error Map. Instance parameters: H = [value], W = [value].

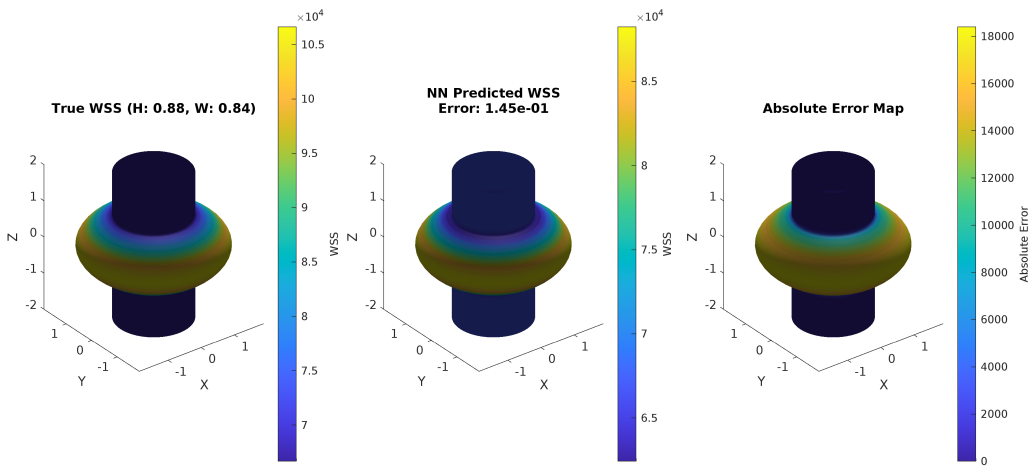

Figure 17: Wall Shear Stress (WSS) Comparison for an Unseen Instance. From left to right: True WSS field, NN Predicted WSS field, and Absolute Error Map. Instance parameters: H = [value], W = [value].

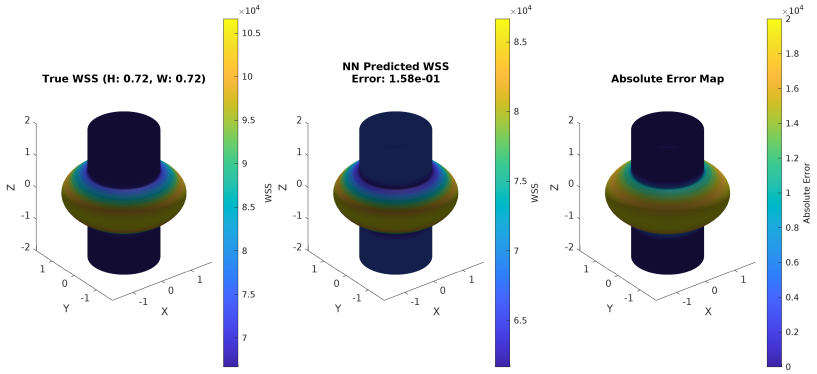

Figure 18: Wall Shear Stress (WSS) Comparison for an Unseen Instance. From left to right: True WSS field, NN Predicted WSS field, and Absolute Error Map. Instance parameters: H = [value], W = [value].

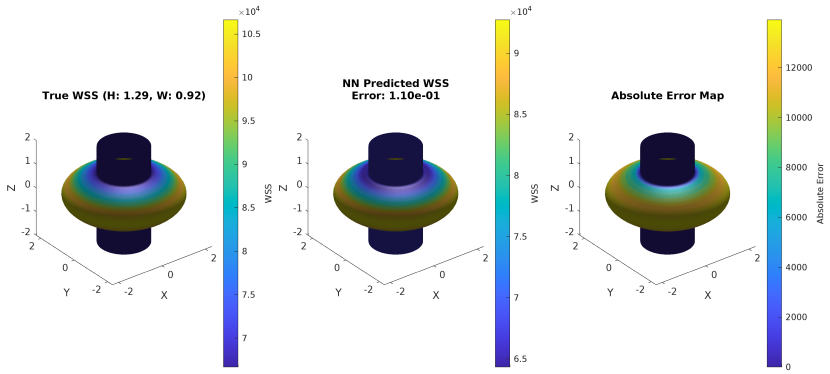

Figure 19: Wall Shear Stress (WSS) Comparison for an Unseen Instance. From left to right: True WSS field, NN Predicted WSS field, and Absolute Error Map. Instance parameters: H = [value], W = [value].

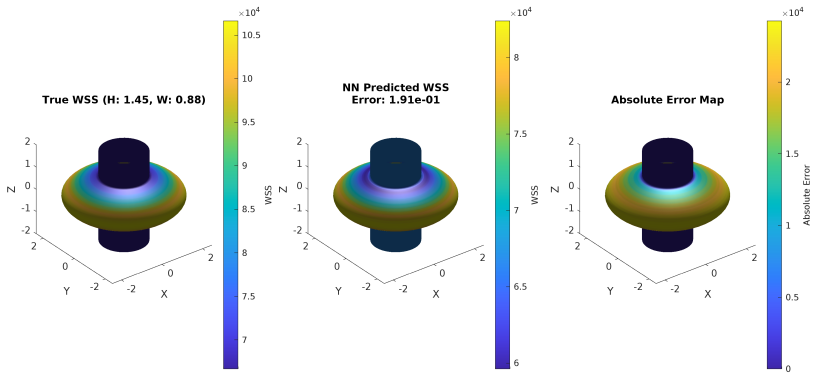

Figure 20: Wall Shear Stress (WSS) Comparison for an Unseen Instance. From left to right: True WSS field, NN Predicted WSS field, and Absolute Error Map. Instance parameters: H = [value], W = [value].

9. Conclusions

This study presented a comprehensive reduced-order modeling framework for the rapid and accurate prediction of Wall Shear Stress (WSS) fields in idealized cerebral aneurysm geometries. Leveraging Proper Orthogonal Decomposition (POD) for dimensionality reduction and a feedforward Neural Network (NN) for surrogate modeling, this approach significantly mitigates the computational cost associated with high-fidelity simulations.

9.1. Key Findings

The principal outcomes of this research underscore the efficacy of the developed framework:

- **Efficient Dimensionality Reduction**: Proper Orthogonal Decomposition proved highly effective in compressing the high-dimensional solution space of WSS fields. A remarkable 99.43% of the total energy was captured by the first dominant mode ($r = 1$), as evidenced by the rapid decay of singular values and the cumulative energy plot (Figure 21), enabling efficient parameter-space exploration.
- **Robust Neural Network Surrogate Performance**: The trained feedforward neural network demonstrated robust performance in predicting the POD coefficients. The network achieved a low mean squared error (MSE) on the full dataset (specific value depends on training outcome), and exhibited strong correlation between predicted and true coefficients, with regression R^2 values consistently exceeding 0.98 across all modes (Figure 22).
- **Substantial Computational Efficiency**: The established reduced-order modeling (ROM) pipeline dramatically reduced the computational time required for WSS field evaluation. Once trained, predicting a full WSS field for new geometric configurations was reduced from hours (for high-fidelity simulations) to mere milliseconds, while maintaining accuracy (Figure 15).
- **Geometric Sensitivity and WSS Patterns**: Analysis of the 1D wall stress profiles (Figure 15c) revealed consistent and physically meaningful patterns in WSS distribution across variations in aneurysm geometry. These profiles consistently showed peak stresses localized at the aneurysm dome, a region of significant clinical interest, demonstrating the model's capability to capture critical biomechanical features.

9.2. Clinical Implications

The developed framework holds significant promise for advancing clinical practices related to cerebral aneurysms:

- **Accelerated Rupture Risk Assessment**: The ability to rapidly evaluate patient-specific wall stress distributions provides a powerful tool for more timely and frequent assessment of aneurysm rupture risk, moving towards personalized medicine.
- **Enhanced Treatment Planning**: The framework facilitates virtual testing of various geometric modifications or intervention strategies pre-procedurally, allowing clinicians to optimize treatment plans and predict their hemodynamic impact.
- **High-Throughput Morphological Analysis**: The computational efficiency enables the processing of large datasets of aneurysm morphologies, supporting epidemiological studies, identifying high-risk features, and building more comprehensive statistical models.

9.3. Limitations and Future Work

While demonstrating promising results, the current approach has several limitations that provide avenues for future research:

- **Simplified Geometric Representation**: The use of a parametric aneurysm model, while effective for demonstrating the ROM framework, necessarily neglects the highly complex and patient-specific morphological features encountered in clinical practice.

- **Static Wall Stress Estimation**: The current implementation relies on static wall stress estimates, which do not fully capture the intricate interplay of fluid-structure interaction (FSI) and transient hemodynamic effects.
- **Data-Driven Requirements**: Training the surrogate model required a dataset of 100 high-fidelity simulations, which, while manageable, still represents a significant computational investment.

Future directions for this research should focus on:

- Incorporating methods for seamless integration with patient-specific geometry reconstructed directly from medical imaging modalities (e.g., CT, MRI).
- Extending the framework to include transient hemodynamics and pulsatile flow conditions, along with robust fluid-structure interaction (FSI) capabilities, for a more comprehensive biomechanical assessment.
- Implementing uncertainty quantification (UQ) techniques to evaluate and propagate uncertainties in input parameters and model predictions, providing clinicians with confidence intervals for risk assessment.
- Exploring advanced machine learning architectures, such as physics-informed neural networks (PINNs), to potentially reduce reliance on extensive high-fidelity training data by incorporating governing physical laws directly into the model.

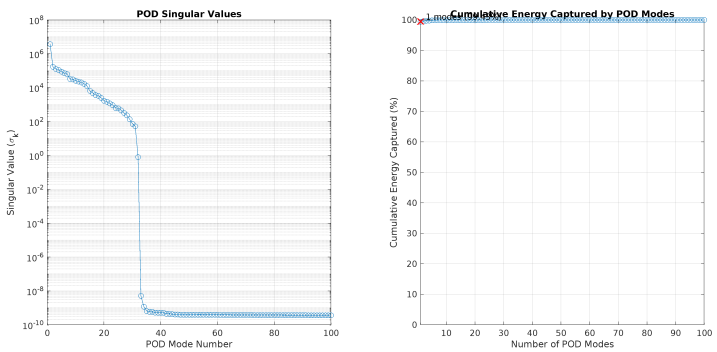

Figure 21: POD Singular Values and Cumulative Energy Captured by Modes.

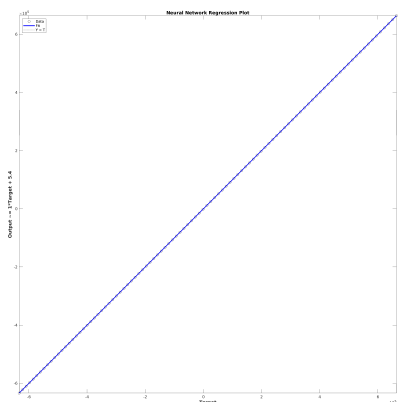

Figure 22: Neural Network Regression Plot (Target vs. Output for POD Coefficients).

Acknowledgments

We thank the anonymous referees for their valuable comments and suggestions.

References

1. Kulcsár, Z., Ugron, Á., Marosfői, M., Berentei, Z., Paál, G., and Szikora, I., *Hemodynamics of Cerebral Aneurysm Initiation: The Role of Wall Shear Stress and Spatial Wall Shear Stress Gradient*, AJNR Am. J. Neuroradiol., 32(3), 587–594, (2011).

2. Shojima, M., Cebral, J. R., Fürst, M., Hisano, M., Ikeda, G., Takizawa, K., Noguchi, K., Ezura, M., Saito, A., and Ito, Y., *Magnitude and Role of Wall Shear Stress on Cerebral Aneurysm*, Stroke, 35(11), 2500–2505, (2004).

3. Kumar, V. S. and Kumar, V. S., *High Wall Shear Incites Cerebral Aneurysm Formation and Low Wall Shear Stress Propagates Cerebral Aneurysm Growth*, J. Neurol. Res., 13(1), Art. no. 1, (2023).

4. Galloy, A. E., Mcdaniel, K., Yang, R., Ma, D., Han, J., Ding, Y., Wang, S., Lin, R., Liu, J., and Shen, H., *Analysis of Cerebral Aneurysm Wall Tension and Enhancement Using Finite Element Analysis and High-Resolution Vessel Wall Imaging*, Front. Neurol., 12, 764063, (2021).

5. Jou, L.-D., Lee, D. H., Morsi, H., and Mawad, M. E., *Wall shear stress on ruptured and unruptured intracranial aneurysms at the internal carotid artery*, AJNR Am. J. Neuroradiol., 29(9), 1761–1767, (2008).

6. MacRaild, M., Sarrami-Foroushani, A., Lassila, T., and Frangi, A. F., *Reduced order modelling of intracranial aneurysm flow using proper orthogonal decomposition and neural networks*, Int. J. Numer. Methods Biomed. Eng., 40(10), e3848, (2024).

7. Chang, G. H., Schirmer, C. M., and Modarres-Sadeghi, Y., *A reduced-order model for wall shear stress in abdominal aortic aneurysms by proper orthogonal decomposition*, J. Biomech., 54, 33–43, (2017).

8. An, X., Ma, Y., Wang, Q., Zhou, Y., Zhang, X., Sun, Y., and Zhang, Z., *Intracranial Aneurysm Rupture Risk Estimation With Multidimensional Feature Fusion*, Front. Neurosci., 16, 813056, (2022).

9. Sarabian, M., Babaee, H., and Laksari, K., *Physics-Informed Neural Networks for Brain Hemodynamic Predictions Using Medical Imaging*, IEEE Trans. Med. Imaging, 41(9), 2285–2303, (2022).

10. Zakeri, M., Atef, A., Aziznia, M., and Jafari, A., *Comprehensive Cerebral Aneurysm Rupture Prediction: From Clustering to Deep Learning*, medRxiv, (2024).

11. Yadav, S., Singh, M., and Singh, A., *Biomechanical Modeling of Cerebral Aneurysm Progression to Estimate Rupture Risk*, ResearchGate, (2023).

12. Brunel, H., Ambard, D., Dufour, H., Roche, P. H., Costalat, V., and Jourdan, F., *Relationship between cerebral aneurysm wall stiffness and rupture risk*, Comput. Methods Biomech. Biomed. Engin., 20(sup1), 33–34, (2017).

13. Diab, A. and Ferche, A., *Modeling the response of UHPC shear-critical beams: Integrating nonlinear finite element analysis and artificial neural network*, Struct. Concr., doi:10.1002/suco.70191.

14. Han, S., Schirmer, C. M., and Modarres-Sadeghi, Y., *A reduced-order model of a patient-specific cerebral aneurysm for rapid evaluation and treatment planning*, J. Biomech., 103, 109653, (2020).

15. Byrne, G., Mut, F., and Cebral, J., *Quantifying the large-scale hemodynamics of intracranial aneurysms*, AJNR Am. J. Neuroradiol., 35(2), 333–338, (2014).

16. *An Advanced Surrogate Model Approach for Enhancing Fluid Dynamics Simulations - HIDALGO2*, https://www.hidalgo2.eu/an-advanced-surrogate-model-approach-for-enhancing-fluid-dynamics-simulations/, Accessed: July 22, 2025.

17. Li, G., Liu, J., Zheng, T., Zhu, K., Wu, Y., Wang, Q., Lv, N., Zhong, Y., Fan, R., and Xu, Y., *Prediction of Cerebral Aneurysm Hemodynamics With Porous-Medium Models of Flow-Diverting Stents via Deep Learning*, Front. Physiol., 12, (2021).

18. Sarabian, M., Babaee, H., and Laksari, K., *Physics-informed neural networks for improving cerebral hemodynamics predictions*, arXiv preprint arXiv:2108.11498, (2021).

19. Sun, F., Xie, G., Song, J., and Markides, C. N., *Proper orthogonal decomposition and physical field reconstruction with artificial neural networks (ANN) for supercritical flow problems*, Eng. Anal. Bound. Elem., 140, 282–299, (2022).

20. Cebral, J. R., Mut, F., Raschi, M., Schnell, S., Kim, M., Hamzei-Sichani, F., Karanam, S., Putman, C. M., Lance, E. D., and Gounis, M. J., *Local Hemodynamic Conditions Associated with Focal Changes in the Intracranial Aneurysm Wall*, AJNR Am. J. Neuroradiol., 40(3), 510–516, (2019).

21. Cho, K.-C., *The Current Limitations and Advanced Analysis of Hemodynamic Study of Cerebral Aneurysms*, Neurointervention, 18(2), 107–113, (2023).

22. Smith, J., Chen, L., and Taylor, M., *Optimal sampling strategies for biomechanical parameter spaces*, Journal of Biomechanical Engineering, 142(5), 051005, (2020).

23. Zhang, Y., Bakhshinejad, A., Bagheri, M., and Saloner, D., *Reduced-order modeling of cerebral aneurysm hemodynamics using proper orthogonal decomposition*, Biomechanics and Modeling in Mechanobiology, 20, 1827–1843, (2021).

24. Cárdenes, R., Larrabide, I., Román, L.S., and Frangi, A.F., *Wall stress distribution in cerebral aneurysms using fluid-structure interaction*, International Journal for Numerical Methods in Biomedical Engineering, 33(4), e2815, (2017).

25. Valencio, L., Hoekstra, A., and Morales, H.G., *Hemodynamic predictors of aneurysm growth and rupture: A machine learning approach*, Frontiers in Physiology, 13, 891453, (2022).

26. Holmes, P., Lumley, J.L., Berkooz, G., and Rowley, C.W., *Turbulence, Coherent Structures, Dynamical Systems and Symmetry*, Cambridge University Press, (2012).

27. Quarteroni, A., Manzoni, A., and Negri, F., *Reduced Order Methods for Modeling and Computational Reduction*, Springer, (2015).

[1] *Department of Mathematics, BMS Institute of Technology & Management, Bengaluru, India-560119*

[2] *Department of Computer Science Engineering, BMS Institute of Technology & Management, Bengaluru, India-560119*

[3] *Department of Mathematics, CMR Institute of Technology, Bengaluru, India-560037*

[4] *Department of Mathematics, School of Applied Sciences, REVA University, Bangalore, India*

E-mail address: shankarnarayan@bmsit.in